Computational Simulations of Bed Surface Variability and Particle Entrainment in a Gravelbed River

Amirreza Ghasemi[1,2], Sanaz Borhani[3], Enrica Viparelli[3], Kimberly M. Hill[1,2]

[1]Department of Civil, Environmental and Geo- Engineering, University of Minnesota, Minneapolis, MN, 55455
[2]St. Anthony Falls Laboratory, University of Minnesota, Minneapolis, MN, 55455
[3]Department of Civil and Environmental Engineering, University of South Carolina, Columbia, SC, 29208

Key Points:

- Bed heights of bedload-dominated rivers modeled by Distinct Element Method (DEM) simulations follow a Gaussian distribution.
- The standard deviation of bed height, s_η, increases as the shear stress increases.
- Peak entrainment of bed particles occurs at a distance $2s_\eta$ above the average bed height.

Corresponding author: Kimberly M. Hill, kmhill@umn.edu

Abstract

We investigate the statistics of bed height variability and particle entrainment height under steady state bedload transport conditions using distinct element method (DEM) simulations. We do so in the context of a theoretical probabilistic formulation derived to better capture spatial variation in sediment exchange between bed material load and alluvial deposits (Parker et al., 2000). Using DEM simulations, we set the foundation for a physics-based closure of this probabilistic framework toward its practical implementation. Towards this, we perform DEM simulations for bedload transport under similar boundary conditions to those of Wong et al. (2007) laboratory experiments: a bed of gravel particles of median grain size 7.1mm with lognormal grain size distribution transported under bed shear stresses ranging from $\tau_0 = 8.70$ to 13.7 Pa. We first validate these simulations by demonstrating that they capture measurable transport and height variations from experimental measurements. We then compute the statistics of both the bed height and entrainment height as they vary with bed shear stress. We find that variabilites in both bed height and entrainment height variabilities follow Gaussian distributions, for which: (1) the standard deviation of bed height variability s_η increases with shear stress, and (2) the peak entrainment height occurs a distance of twice the standard deviation of bed height variability ($2s_\eta$) above the mean bed height. We discuss implications of these results and next steps for understanding these transport statistics under a broader range of conditions.

1 Introduction and Background

Predicting the evolution of alluvial channels is a significant problem for environmental restoration and also for adaptation under ever-changing climate conditions. To predict spatial and temporal evolution of alluvial channels, modelers combine (1) equations expressing the conservation of mass and momentum of the fluid flow (e.g., Saint-Venant equations, or similarly well-known representations); (2) equations expressing the conservation of mass along the sediment bed surface (e.g., the Exner equation), and (3) equations expressing a dependence of particle transport on average fluid stress on an alluvial bed (e.g,. by Meyer-Peter and Muller (1948), Ashida and Michiue (1972), Wilcock and Crowe (2003)). This paper is concerned with the manner in which we relate spatial gradients in sediment transport with temporal height changes in a sediment bed, primarily associated with (2) above. For this we turn what is often called "the Exner Equation," essentially conservation of sediment mass.

1.1 Conservation of Sediment Mass: The Exner Equation

In its simplest form, assuming uniform particle density and constant solid fraction throughout of the bed, the Exner equation can be expressed as:

$$(1-\lambda_p)\frac{\partial \eta(x,t)}{\partial t} = -\frac{\partial q(x,t)}{\partial x} \tag{1a}$$

$$(1-\lambda_p)\frac{\partial \eta(x,t)}{\partial t} = D(x,t) - E(x,t) \tag{1b}$$

Here, q is the volumetric transport rate of sediment per unit width. We use x as the direction of average transport, so $\partial q/\partial x$ is the spatial gradient of sediment transport downstream. If negative, then it contributes to a growth in local bed height, η, over time t (Fig. 1(a)). λ_p is the bed porosity. As indicated, the Exner Equation is sometimes expressed in what is typically called the *entrainment form* using the difference between local rates per area of deposition D and entrainment E. While either form provides an extraordinarily efficient way to capture average elevation changes in a sediment bed, nei-

ther has the functionality to reflect any variations associated with grain size distributions, nearly universal in natural rivers.

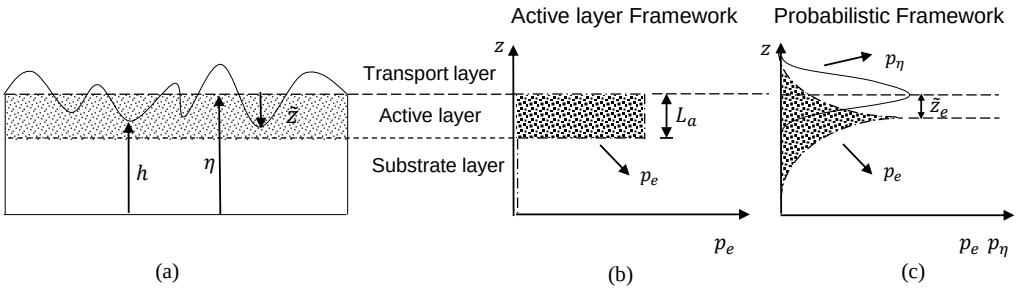

Figure 1. Schematic representation of a sediment bed illustrating particular variables in the model frameworks described in this paper. (a) a representative sketch of a bed, (b) Discrete model with *active layer* formulations, and (c) continuous model proposed by Parker et al. (2000).

1.2 The Active Layer-Based Exner Equation

To efficiently account for the non-uniformity of the bed material grain size, morphodynamic models generally express mass conservation of sediment particles with the aid of the active layer approximation (Hirano, 1971; Parker, 1991b, 1991a). Examples include downstream fining in rivers (Parker, 1991b, 1991a), the long-term evolution of a gravel-sand transition (Ferguson, 2003), sedimentation in lakes and reservoirs (Cui, Parker, et al., 2006; Cui, Braudrick, et al., 2006) and the prediction of grain size stratigraphy in an alluvial deposit (Ribberink, 1987).

An active layer-based model includes explicit consideration of a finite-thickness interface layer between particles in transport and bed deposit. Thus, the bed deposit is divided in two parts: the interface or active layer and the substrate. In tracking the concentration of one particle type i (e.g., color only, density, or size), we can write the active-layer version of the (entrainment form) Exner equation as:

$$(1-\lambda_p)\left[f_{L,i}\frac{\partial \eta}{\partial t}+(f_{a,i}-f_{L,i})\frac{\partial L_a}{\partial t}+L_a\frac{\partial f_{a,i}}{\partial t}\right]=D_i-E_i \tag{2}$$

L_a is the active layer thickness (Fig. 1(b)); $f_{L,i}$ is the volume fraction of particles of type i in the active layer at the interface of the active-layer with substrate, and $f_{a,i}$ is the volume fraction of particles of type i in the active layer. D_i and E_i represent volumetric sediment deposition rate and sediment entrainment rate, respectively, per unit area. Porosity λ_p is approximated as uniform from the bottom of the transport layer and active layer and throughout the substrate. The volume fraction of particles of type i in the active layer is approximated as uniform.

This model framework tracks entrainment and deposition of a particular grain type i in substrate-transport exchange translated somewhat through the finite-thickness active layer. For example, during a depositional period, the grain size characteristics of the particles in transport do not necessarily equal the characteristic of the top of the bed. Rather, the characteristics of the sediment transferred to the substrate during deposition are generally a combination of that in the active and transport layers and are assigned in a manner that can differ from one model to the next (Ferguson, 2003).

While this framework captures some aspects of grain size segregation and associated stratification that occur during depositional processes at the associated timescales, it does not have the capability to account for exchanges that can happen due to grain size effects with what can be somewhat shorter timescales. An example of this occurs when smaller particles in a mixture find "pockets" in a bed at a statistically higher rate than do larger neighboring particles and push the larger particles into transport through a "squeeze-expulsion" mechanism (Savage & Lun, 1988). This time scale of this process depends more on the particle dynamics time scales than it does depositional scales and thus cannot be fully captured through the active layer model.

Under equilibrium conditions, restrictions of the active-bed layer formalism become even more apparent. The exchange of sediment among layers can only be associated with changes in the mean bed elevation. During steady conditions ($\partial q/\partial x = 0$, and $D = E$) this framework predicts no exchange at all between substrate, active, and transport layers (Viparelli, Haydel, et al., 2010; Viparelli, Sequeiros, et al., 2010). Also, the discrete representation of the deposit limits entrainment and deposition to the topmost part of the bed. In summary, active layer-based models cannot account for vertical sediment fluxes associated with bedform migration, cannot reproduce the infiltration of fine particles in a coarse substrate, fail to reproduce the fine details of the alluvial stratigraphy and cannot capture tracer and contaminant dispersal (Blom et al., 2008; Parker, 2004; Pelosi et al., 2014).

2 Theoretical Approach: Probablistic Exner Equation

Towards a solution to the problems of the layer-based Exner equation, Parker et al. (2000) proposed a continuous framework that eliminates the discretization associated with transport-substrate interfaces. At the same time, it allows for variable particle sizes and other characteristics. While this framework is both efficient and flexible, there are unresolved closure problems we address herein. The equation of conservation of sediment volume at elevation z in the deposit for the case of uniform material takes the form:

$$(1-\lambda_p)p_\eta(x,z,t)\frac{\partial \eta(x,t)}{\partial t} = p_d(x,z,t)\times D - p_e(x,z,t)\times E \tag{3}$$

p_η is a height-dependent probability density, essentially, the probability that the instantaneous (or local) bed elevation is at height z at time t. p_d and p_e are the probability densities that account for bed-normal, depth dependent deposition and entrainment rates.

This probabilistic form of the Exner equation allows for bedload-substrate particle exchange below (or above) the average bed surface, common in cases of bed surface variability associated with roughness, bedforms, etc. (as in Fig. 1). In other words, the bed-normal depth dependences of p_d and p_e represent expected variability in deposition and entrainment associated with short term changes of local bed level associated with sediment transport processes as particles are alternately plucked from and deposited into the bed (Figure 1). The form allows for segregation in mixtures with significant spatial variability (bed roughness and bedforms). And the form allows for bedload-bed exchange under steady state. This framework offers all this without need to explicitly represent short-term variability. However, for its application to alluvial problems, the framework needs closure, in other words, functional forms for p_d, p_e, and p_η.

Wong et al. (2007) took the first significant steps toward testing the probabilistic framework and deriving expressions for p_d, p_e, and p_η. They performed laboratory flume experiments using gravel particles of a narrow, lognormal size distribution (Table 1). They performed experiments under steady state, lower-regime plane-bed conditions. To find p_η, they used a sonar-transducer system to measure local time-dependent bed elevations. In doing so, they found that p_η follows a Gaussian distribution whose standard deviation s_η depends on bed shear stress τ_o:

$$p_\eta(z|\eta, s_\eta^2) = p_\eta(\tilde{z}|0, s_\eta^2) = \frac{1}{\sqrt{2\pi}s_\eta(\tau)} exp\left[-\frac{1}{2}\left(\frac{\tilde{z}}{s_\eta(\tau)}\right)^2\right] \tag{4}$$

Here, following Wong et al. (2007), $\tilde{z} = \eta - z$ (see Fig. 1(a)). Unfortunately p_d ($= p_e$ in steady state conditions) were inaccessible directly due to the opacity of the particles and associated difficulty of identifying initial particle movement and the associated height just prior to that movement. Instead, based in part on depth-dependent entrainment of tracer particles, Wong et al. (2007) proposed an elevation-specific density for entrainment from their data:

$$p_d(\tilde{z}) = \frac{1}{2s_\eta(\tau)} exp\left(-\frac{|\tilde{z} - \tilde{z}_e - \tilde{z}_n|}{s_\eta(\tau)}\right) \tag{5a}$$

$$p_e(\tilde{z}) = \frac{1}{2s_\eta(\tau)} exp\left(-\frac{|\tilde{z} - \tilde{z}_e + \tilde{z}_n|}{s_\eta(\tau)}\right) \tag{5b}$$

$\tilde{z}_e$ is an offset Wong et al. (2007) suggested characterizes steady state conditions (i.e., mobile-bed equilibrium). They proposed that maximum entrainment was likely to occur just below the average bed surface ($\tilde{z}_e \geq 0$). $\tilde{z}_n$ an additional offset function that characterizes non-equilibrium conditions. Their experimental data suggest $\tilde{z}_e = 0.25d_{50}$ (Here, d_{50} is the median grain size.) Since their experiments involved equilibrium conditions, no value for $\tilde{z}_n$ was available.

These experimental data provided the confidence that this framework would be effective in capturing depth-dependent phenomenology in bedload transport conditions. However, physical experiments to gather the additional data needed to close the equations are extremely limited. Measurements of bed height such as those performed by Wong et al. (2007) are limited to the absolute local surface of particles and cannot distinguish between moving particles and particles in the bed. Modern techniques such as index-matched tracking of subsurface particles show promise but at present have not been performed to address these issues.

In this paper, we aim to close the probabilistic Exner equations using computational simulations based on the distinct element method (DEM). In DEM simulations, we can track the motion of each particle at every time step and thus can provide robust particle location and velocitiy at each time step toward the derivation of local bed height and elevation-specific erosion and deposition densities. Additionally, since different effects can be "turned on" and "turned off" in DEM simulations, we can systematically explore the importance of specific system details, including grain size distribution, grain shape, average stress on the bed, and turbulent fluctuations.

The rest of the paper is organized as follows. In the next section, we introduce our computational set-up including details such as grain size distribution, fluid velocities, and subsequent analysis methods. In the results section, we present data demonstrating that this simple model performs well in comparison with established bedload relationships as well as statistical experimental data such as those of Wong et al. (2007). In the discussions section we present more details on the data including a remarkably simple scaling relationship between entrainment height statistics and bed surface variability under steady conditions. We conclude this paper with a brief summary and discussion of necessary extensions of this work, for example, to cases of different grain size distributions, inclusion of turbulence fluctuations, and non-equilibrium transport conditions.

3 Distinct Element Method (DEM) Simulations

Toward determining how the statistics of bed height and entrainment height vary with shear stress on an alluvial bed, we performed computational Distinct Element Method (DEM) (Cundall & Strack, 1979) experiments we designed to have similar conditions to the physical experiments performed by Wong et al. (2007) in terms of grain size distribution and fluid properties (Table 1) and bed shear stress (Table 2). In this well-established technique, the motion of each particle in the system is tracked throughout the simulation. We can directly incorporate particle sizes, densities, and elasticities using Hertz-Mindlin interparticle interactions (Hertz, 1882; Tsuji et al., 1992), and can model fluid forcing and other boundary conditions through other parameters as we describe presently.

3.1 Our DEM Model

Our DEM simulations are built on an in-house DEM model similar to that of Hill and Tan (2017). To model the translational and rotational motion of each particle we use the following relationships:

$$m_i \frac{d\vec{u}_i}{dt} = \Sigma_j \vec{F}^c_{ij} + \Sigma_k \vec{F}^{nc}_{ik} + \vec{F}^f_i + \vec{F}^g_i \tag{6a}$$

$$I_i \frac{d\vec{\omega}_i}{dt} = \Sigma_j \vec{M}_{ij} \tag{6b}$$

m_i, $\vec{u}_i$, I_i, $\vec{\omega}_i$ are the near-instantaneous mass, velocity, moment of inertia and rotational velocity, respectively, of particle i. $\vec{F}^c_{ij}$ and $\vec{F}^{nc}_{ik}$ represent interparticle forces on particle i due to contacting and non-contacting particles. $\vec{F}^c_{ij}$ represent the force from particle j on particle i due to direct contact and thus the form reflects the model response to deformation associated particle properties (Section 3.1.1); $\vec{F}^{nc}_{ik}$ represents non-contact interactions from particle k on particle i such as those that mediate particle-fluid interactions. $\vec{F}^f_i$ concerns the fluid forces on particle i (Section 3.1.2). $\vec{F}^g_i = m_i\vec{g}$ is the weight of particle i. $\vec{M}_{ij}$ represents the force moments on particle i by particle j associated with the interparticle forces.

3.1.1 Interparticle Contact Force Model

We model the interparticle contact forces (the first term on the right hand side of Eq. 6a) using the Hertz-Mindlin (Hertz, 1882; Mindlin, 1949) contact theory with a damping component and Coulomb sliding friction:

$$F_n = -k_n {\delta_n}^{3/2} - \eta_n {\delta_n}^{\frac{1}{4}} \dot{\delta}_n \tag{7a}$$

$$F_t = \min[-k_t {\delta_n}^{\frac{1}{2}} \delta_t - \eta_t {\delta_n}^{\frac{1}{4}} \dot{\delta}_t, -\mu F_n \delta_t / |\delta_t|] \tag{7b}$$

As is standard (e.g., Tsuji et al. (1992)), δ_n and δ_t are model deformations in the normal and tangential directions relative to the contact plane. F_n and F_t are forces in the normal and tangential directions, respectively. Here and throughout the paper, $\dot{q}$ represents temporal derivatives in any variable q. k_n and k_t are stiffness factors, and η_n and η_t represent damping factors, all of which can be calculated based on particles characteristics such as particle size, mass, and Young's moduli (See Appendix A).

3.1.2 Fluid Force Model

Similar to Schmeeckle and Nelson (2003), at each time step we calculate the fluid force $\vec{F}^f_i$ on each particle i according to:

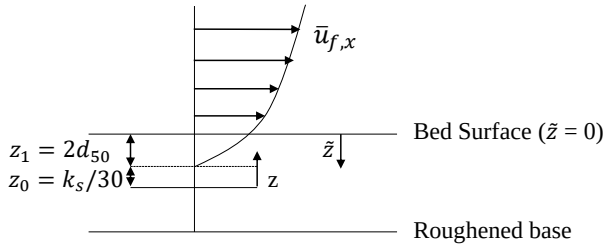

Figure 2. Sketch of flow velocity profile of the simulated bedload transport.

$$\vec{F}_i^f = \vec{F}_{bi} + \vec{F}_{mi} + \vec{F}_{di} \tag{8}$$

$\vec{F}_{bi} = -\rho_f \forall_i \vec{g}$ denotes the buoyancy force; ρ_f is the fluid density, $\forall_i$ is the volume of particle i. $\vec{F}_{mi} = \rho_f \forall_i c_m \dot{\vec{u}}_i$ is an "added mass force"; $\vec{u}_i$ is the instantaneous velocity of particle i, c_m is an empirically determined coefficient – we use $c_m = 0.5$ as suggested by Batchelor (1976) and Drake and Calantoni (2001). $\vec{F}_d = \frac{1}{2}\rho_f c_d A_i |\vec{u}_{\mathrm{rel},i}| \vec{u}_{\mathrm{rel,i}}$ denotes the drag force, where $A_i = \pi d^2/4$ is the central cross-sectional area of the particle i, $\vec{u}_{\mathrm{rel},i}$ is the local fluid velocity relative to that of the particle i, and c_d is a drag coefficient suggested by Drake and Calantoni (2001):

$$c_d = 24 {Re_p}^{-1} + 4 {Re_p}^{-0.5} + 0.4 \tag{9}$$

$Re_p = |\vec{u}_{\mathrm{rel}}| d/\nu$ is a particle Reynolds number, and $\nu = 10^{-6} m^2/s$ is the kinematic viscosity of water at room temperature (Table 1).

3.1.3 Model Bed Shear Stress, Fluid Velocity, and Shielded Fluid Velocity

Our representation of bed shear stress τ_o relies on the well-known expression for what is known as the "log-law of the wall", a mathematical expression of the average streamwise fluid velocity profile $\overline{u}_{f,x}(z)$ observed under steady turbulent conditions:

$$\overline{u}_{f,x}(z) = \frac{u_\tau}{\kappa} ln\Big(\frac{z}{z_0}\Big) \tag{10a}$$

$$z_0 = k_s/30 = 3.5 d_{50}/30 \tag{10b}$$

In this equation, $u_\tau \equiv \sqrt{\tau_o/\rho_f}$ is the shear velocity, $\kappa = 0.41$ is the von Karman constant, and z_0 is the position at which the fluid velocity is zero ($\overline{u}_{f,x}(z_0) = 0$). As relatively common, we define z_0 in terms of a roughness coefficient, k_s, that scales with a representative particle diameter (e.g., Pope (2001), Schlichting and Gersten (2016), van Rijn (1982)). We dynamically locate the position at which $\overline{u}_{f,x}(z) = 0$ so that the distance between the bed surface and the zero-fluid-velocity plane is $z_1 = 2d_{50}$, as in Fig. 2. (computational details in Section 3.3).

For the work we describe in this paper, we do not explicitly model turbulent (fluctuating) velocities so that $u_{\mathrm{rel},y} = -u_y; u_{\mathrm{rel},z} = -u_z$ where u_y and u_z are the components of particle velocity in cross-stream and vertical directions, respectively. While we limit ourselves to one-way coupling for the work described here, we include some shielding effect from upstream particles that theoretically influences the drag force experienced

Table 1. Summary of fluid and particle properties.

Property	Magnitude
fluid density ρ_f	1000 kg/m^3
fluid kinematic viscosity	10^{-6} m^2/s^2
particle size (d_{50}, d_g, σ_g)	(7.1 mm, 7.2 mm, 1.2)
particle density ρ_p	2650 kg/m^3
particle elastic modulus E_p	29 GPa
particle Poisson's ratio ν_p	0.2

by each particle in the downstream. For this, we use the experimentally-derived relationship proposed by Schmeeckle and Nelson (2003):

$$u_{\mathrm{rel},x} = [\overline{u}_{f,x}(z_c) - u_x] \times \mathrm{erf}\left(\frac{l_d - h_p}{5h_p}\right) \tag{11}$$

In this equation, $\overline{u}_{f,x}(z_c)$ is the fluid velocity from Eq. 10a (Fig. 2) at a particular particle center z_c, u_x is the downstream particle velocity, l_d is the downstream distance between the center of the particle of concern and its first upstream neighbor, and h_p is the height difference between the topmost part of the two particles.

3.2 Computational Experiment Parameters

Toward validating our computational experiments with physical experiments by Wong et al. (2007), we choose our force parameters to reflect properties of hard rock particles (i.e. granite) with narrow log-normal distribution. In regards to fluid flow, we use the properties of water for the fluid and vary the bottom shear stress τ_o so that the Shields number ($\tau^* = \tau_o/((\rho_s - \rho_f)gd_{50})$) ranged from $\tau^* = 0.0757$ to 0.1193.

We design the channel to have periodic boundary condition in the downstream and transverse directions ($x-$ and $y-$ directions, respectively). To ensure our results are not size limited, we performed various simulations on different size channels (Fig. 3b). Based on these which show that stable conditions occur with a minimum channel length of $\approx$ 50 d_{50}, we designed our channel for the results reported here to be 350 mm long and 85 mm wide. For most of the simulations we performed here (table 2), we used the same number of particles N=3000, resulting in a bed with the height of approximately five d_{50}. We found this to be a sufficient number of particles (and bed height) so that the results were not affected by this relatively small height (e.g., as compared with runs of 10,000 particles and 15,000 particles in runs 3a and 3b in Table 2, respectively).

3.3 Simulation Initialization and Outputs

To initialize each computational experiment, we start with the randomly-arranged particles above the bed. We release these particles and allow them to settle to the bed. During this period, the forces are limited to gravity and contact forces. Under gravitational forces, the particles drop to the bed. As some of the particles rebound from the bed, they collide with other falling particles resulting in somewhat randomized positions and velocities as the particles settle down.

Based on the sum of all forces on each particle, we calculate its translational acceleration at each time step, and, based on the sum of all surface forces, we calculate its rotational acceleration (Eq. 6). We integrate these accelerations using the fourth-order runge-kutta method (Chapra et al., 2010) at each time step to update each particle's trans-

Table 2. Computational flow and bed parameters.

Run	Bed thickness	N	τ^*	k_s	z_1
1	$\sim 5d_{50}$	3000	0.1193	$3.5d_{50}$	$2d_{50}$
2	$\sim 5d_{50}$	3000	0.1052	$3.5d_{50}$	$2d_{50}$
3	$\sim 5d_{50}$	3000	0.1044	$3.5d_{50}$	$2d_{50}$
3a	$\sim 16d_{50}$	10000	0.1044	$3.5d_{50}$	$2d_{50}$
3b	$\sim 25d_{50}$	15000	0.1044	$3.5d_{50}$	$2d_{50}$
4	$\sim 5d_{50}$	3000	0.0915	$3.5d_{50}$	$2d_{50}$
5	$\sim 5d_{50}$	3000	0.0908	$3.5d_{50}$	$2d_{50}$
6	$\sim 5d_{50}$	3000	0.0844	$3.5d_{50}$	$2d_{50}$
7	$\sim 5d_{50}$	3000	0.0757	$3.5d_{50}$	$2d_{50}$

[a] N is the number of particles.

lational and rotational positions and velocities. Each computational time step is approximately 5 μs. To save computational time and space, we output particle locations and velocities every 10,000 time steps i.e., every 50 ms

After the initial drop of the particles, they settle and stop moving. Once the particles reach this state, we "roughen" the bed with the particles touching the base of the channel. That is, we affix these particles to this bottom surface to avoid sliding between the particles and the channel base that would otherwise occur under the fluid forcing. We use this same initialized bed for all simulations performed here to minimize additional uncertainties that might be introduced by local variations in bed roughnesses. Once the particles in this roughened bottom bed are fixed in place, we "turn on" the fluid forces (Eq. 8) associated with the fluid flow (Eq. 10a).

To initialize the fluid flow we need to determine the location of the bed surface ($z = z_0 + z_1$ in Fig. 2). Towards this, we first consider the particle location data from five equal-sized vertical bins in the simulated flume, each 70 mm long and 85 mm wide. From these five sets of data, we determine the location of the highest particle in each column, and set the average of these five heights to be the location of $z = z_0 + z_1$ for the fluid velocity profile.

Once we have initiated the fluid velocity, at every time step we calculate all interparticle and fluid forces on each particle (Eq. 7 and Eq. 8). The particles on the surface start to move, primarily by rolling and also by hopping along the bed surface. As the particles move, the height of the top-most particles change. To account for this we dynamically adjust the vertical position of the velocity profile. We do so similarly to our fluid initialization process. We again consider particle data from five equal-sized vertical bins. Though, here we consider particles only whose velocities are smaller than the local fluid velocity. We average the position of the top-most particle in each bin that meets that criteria to define the new location of $z = z_0 + z_1$.

Once the fluid is initialized, we continuously use the particle positions and velocities to calculate transport rate, bed height statistics, and entrainment statistics. As we describe in section 4.1, after fluid intialization, we find the system reaches steady state in ≈ 2.5 s. We report our statistical results calculated for 20 s of steady state run conditions.

4 Results and Implications for the Probabilistic Exner Formulation

4.1 Transport Rate

We calculate a spatially-averaged near-instantaneous unit transport rate q_{t_i} at output timestep t_i according to:

$$q_{t_i} = \frac{\sum_{p=1}^{N} \forall_p u_{p,x}(t_i)}{\text{bed area}} \tag{12}$$

In this equation, $u_{p,x}(t_i)$ is the velocity of particles p at output time step t_i in the downstream direction (if t is the simulation time in seconds after the water is "turned on", $t_i = t * 20$); $\forall_p$ is the volume of that particle, N is the number of particles ($N = 3000$ for most of the results reported here), and the bed area for most of the data reported here is 350 mm × 85 mm, or ≈ 50 d_{50} × 12 d_{50}. As is common, we non-dimensionalize our transport rate according to:

$$q^* = \frac{q}{\sqrt{(s-1)g d_{50}} d_{50}} \tag{13}$$

often referred to as the Einstein number. Typical for systems in bedload transport, there is a high temporal variability in the transport rate (Fig. 3(a)). So, for comparison with experiments, we define the average dimensionless transport rate from $t = t_s = 2.5$ s to time $T = t - t_s$ as q^*_T:

$$q^*_T = \frac{\sum_{t_i=t_s\times 20}^{t_i=(T+t_s)\times 20} q^*_{t_i}}{T \times 20} \tag{14}$$

In this equation, the factor of 20 is associated with the rate of 20 outputs per second. Based on data such as those plotted in Fig. 3(a, inset), we used $T = 20$ as a sufficiently long time to average the fluctuations for clear results. Henceforth, we use $q^* \equiv q^*_{20}$ to represent a statistically steady average unit transport rate for each system.

To compare our transport data from those previously published for similar systems, we note that for a number of well-known bedload transport relations (e.g., Meyer-Peter and Muller (1948); Luque and Van Beek (1976)), q^* scales roughly as $\tau^{*1.5}$:

$$q^* = a_q \times (\tau^* - \tau^*_c)^{1.5} \tag{15}$$

Here, τ^*_c is an empirically determined reference stress below which the transport rate is negligible. To compare our results to these published relationships, we calculate the linearized least squares fit of Eq. 15 to our data. Fig. 4(a) demonstrates that our data are well-fit by this equation when $a_q \approx 2.59$ and $\tau^*_c \approx 0.051$. As we discuss shortly (Section 5), our results are particularly close to those from the physical experiments by Wong et al. (2007) after which we patterned our simulations (Fig. 4(b) and caption).

4.2 Bed Surface Statistics

To calculate the bed surface and entrainment statistics, we need to quantitatively distinguish between "bed particles" and "entrained particles". To do so, we consider theoreticl forms of average particle velocity in bedload transport, from Bagnold (1956) and Bridge and Dominic (1984) (and references within):

$$u_{p,a} = a_u \times (u_\tau - u_{\tau c}) \tag{16}$$

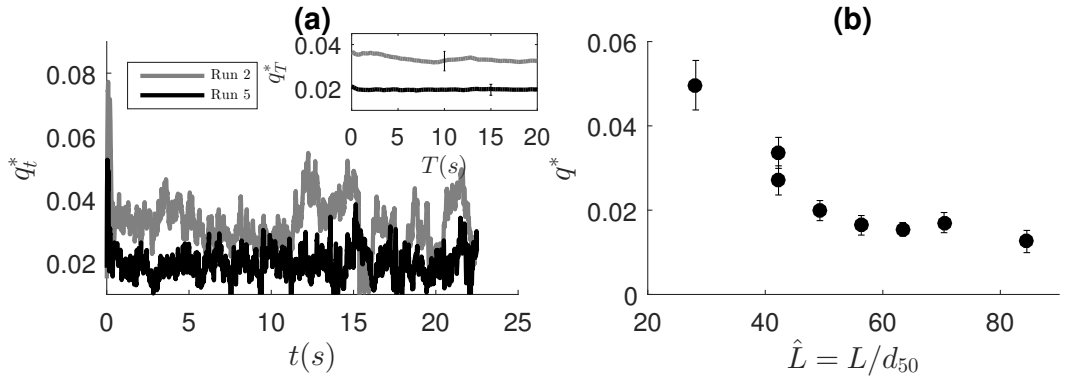

Figure 3. The conditions required to perform statistical analyses of bed surface: (a) shows the time needed to reach steady state conditions. The inset shows the average transport rate starting just after reaching steady state to time T after reaching steady state. The error-bar in the inset shows the standard deviation of transport variations for 20 seconds after reaching the steady state conditions. (b) shows the minimum channel length required to eliminate the effect of channel size on the transport rate. q^* represents the average transport rate for 20 seconds after reaching the steady state.

Here, $u_\tau \equiv \sqrt{\tau_0/\rho}$ is the shear velocity, $u_{\tau c} \equiv \sqrt{\tau_c/\rho}$ is a reference shear velocity, and a_u is a coefficient that researchers typically treat as constant, ranging from approximately 8.5 (e.g., Bagnold (1956)) to 14 (e.g., Abbott and Francis (1977)).

We determined that using $a_u = 5$ provides reasonable results to quantitatively distinguish between bed particles and entrained particles (e.g., Fig. 5). So we defined a *threshold* velocity that distinguishes between moving and stationary particles:

$$u_{\text{th}} \equiv u_{p,5} \equiv 5 \times (u_\tau - u_{\tau c}) \tag{17}$$

Toward calculating our bed surface variability, we divided the channel into 150 subsections (each a column of cross-sectional area $\approx 14\ mm \times 14\ mm \approx 2\ d_{50} \times 2\ d_{50}$). For the jth column, at each time step t_i we record the top of the upper-most stationary particle (whose downstream velocity was less than u_{th}): $z_{top,i,j}$. We defined the averaged bed surface height η as the arithmetic mean of those (600,000) values and calculated what might be considered an effective bed roughness as the standard deviation of the mean.

For a visualization of how the standard deviation varies with shear stress, we define a variance of each bed height as $\tilde{z}(x_j, y_k, ti) \equiv \eta - z_{top}(x_j, y_k, ti)$. Then we divide these data into 10 bins of equal width ($\Delta\tilde{z}$) ranging from the lowest to highest values of $\tilde{z}$ throughout each experiment. We normalize these binned data and then plot them in Fig. 6 for three representative simulations of different shear stresses. From these plots, we can see that, while not perfect in all cases, a Gaussian distribution fits the data well, as suggested by analogous experimental data of Wong et al. (2007).

Similar to the results of Wong et al. (2007), the bed roughness of our simulation data increases with increasing bed shear stress (τ_0). We plot the standard deviation of the bed heights (s_η) normalized by d_{50} ($\hat{s}_\eta = s_\eta/d_{50}$) versus Shields stress (τ^*) in Fig. 7. We find a power law relationship between the two:

$$\hat{s}_{\eta,\text{fit}} = a_\eta(\tau^* - \tau^*_c)^{b_\eta} \tag{18}$$

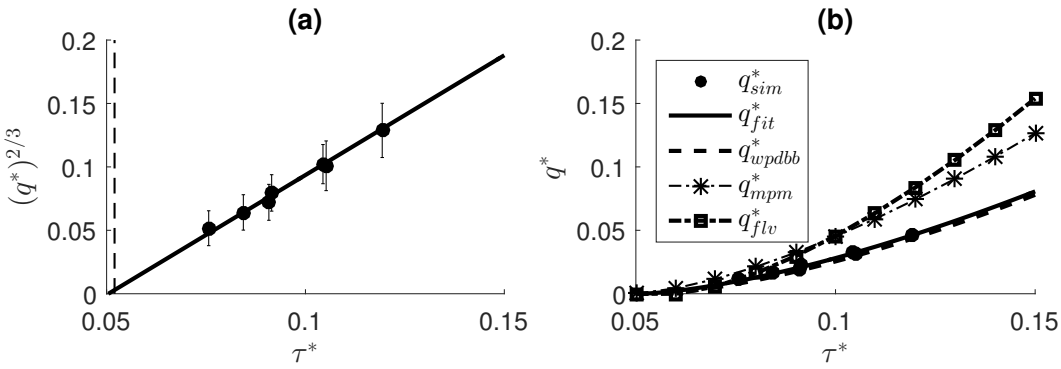

Figure 4. a) Our data for $q^{*2/3}$ plotted vs. τ^* (solid circles) and a linearized least squares fit of Eq. 15 (line) to those data $[a_q,\tau_c^*]$=[2.59, 0.051]. Vertical dashed line: the reference Shields stress calculated using the Brownlie equation: $0.22Re_p^{-0.6} + 0.06 \times 10^{(-7.7Re_p^{-0.6})}$. b) q^* plotted vs. τ^* for our data (q^*_{sim}) (solid circles) and the fit from (a) (solid line) compared with other previously proposed relationships. q^*_{wpdbb} is the fit proposed by Wong et al. (2007), $[a_q,\tau_c^*]$=[2.66, 0.0549]; q^*_{mpm} is from the well-known transport model proposed by Meyer-Peter and Muller (1948), $[a_q,\tau_c^*]$=[3.97, 0.0495], modified by Wong and Parker (2006); q^*_{flv} is the transport model proposed by Luque and Van Beek (1976), $[a_q,\tau_c^*]$=[5.7, 0.06].

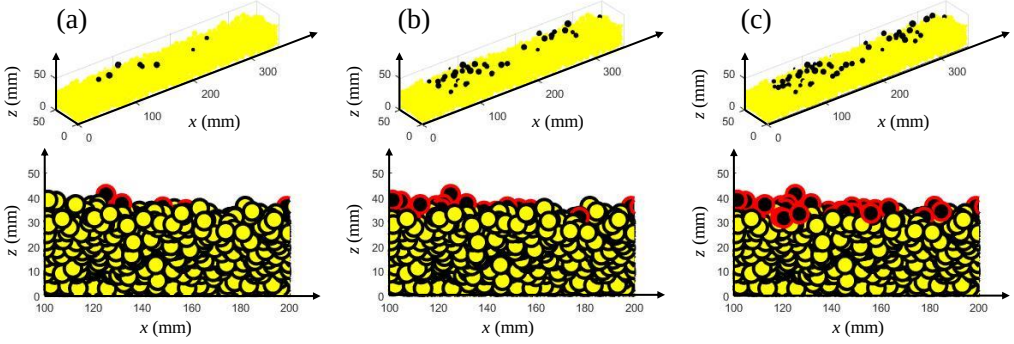

Figure 5. Schematic representation of simulated particles in 3D (top row) and 2D (bottom row) to illustrate the effect of changing a_u on the threshold velocity described in the text which is used to distinguish between stationary and moving particles. The dependence of moving particles (black color) number on the threshold velocity: a) $u_{\rm bd} < u_{\rm p,5}$, b) $u_{\rm bd} < u_{\rm p,2}$, c) $u_{\rm bd} < u_{\rm p,1}$. Here $u_{\rm bd}$ is the velocity of bed particles.

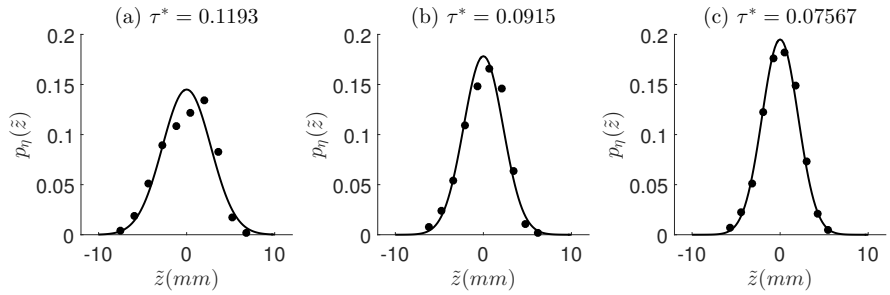

Figure 6. Three representatives of probability density distribution of bed height variations. Filled circles represent the simulation data while the solid line represents the Gaussian fitting curve, $p_{\eta,gau}(\tilde{z}|0, s_\eta^2)$. Table 3 shows the standard deviation of these fittings for all the computational experiments designed for this study.

Again, τ_c^* is the reference shear stress derived from the transport data, (Eq. 15). This form is not unlike that suggested by the experimental data of Wong et al. (2007), as we discuss in Section 5.

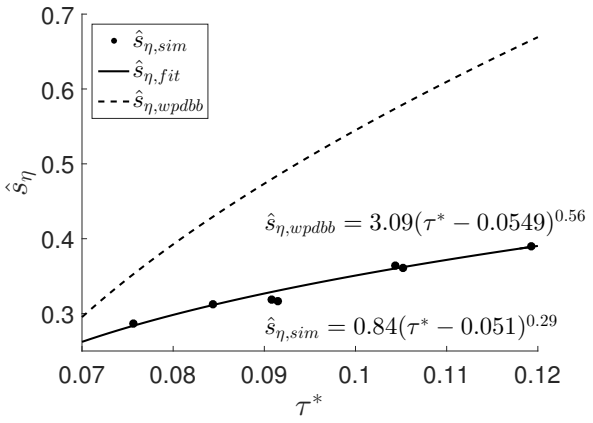

Figure 7. Power law fitting model for standard deviation of bed height variation against Shields stress. Filled circles represents the calculated standard deviation from the simulations. Solid line represents our fitting model with $a_\eta = 0.84$ and $b_\eta = 0.29$ while the dashed line represents the fitting model suggested by Wong et al. (2007) with $a_\eta = 3.09$ and $b_\eta = 0.56$

We note at this point we found no noticeable differences in the bed surface variations when we double and triple the bed height (as in Run 3 compared with Run 3*a* and 3*b*), so we focus on analyzing the results only for the 3000 particle simulations for the rest of this paper.

4.3 Particle Entrainment Statistics

For a quantitative measure of the entrainment height statistics for our data, we first need to clearly define what we identify as an entrainment event, that is, a "conversion" of a bed particle to an entrained particle. Since a particle is not typically considered entrained if it moves only a short distance, such as that limited to shaking or rocking, we base a quantitative definition on a minimum distance that a particle must travel in a cer-

tain amount of time before we consider it to be entrained. What constitutes a minimal distance to be considered entrained in a general sense is debatable and warrants discussion beyond the scope of this paper. For our purpose, we consider a particle entrained if it travels at an average speed greater than $u_{\rm th}$ (Eq. 17) for a half second. In other words, its minimum displacement once entrained is:

$$\delta r_{min} = u_{\rm th}\delta t \tag{19}$$

where $\delta t = 0.5\ s$. For each entrainment event defined in this way, we use the vertical position of these particles relative to the mean bed height, $\tilde{z}$, prior to their entrainment for entrainment height statistics. We bin these data and normalize them as we did for the bed height data and plot the distributions for three representative shear stresses in Fig. 8. For an analytical expression of the probability of entrainment heights, we consider two, the exponential form previously suggested (Eq. 5b) and a normalized Gaussian distribution:

$$p_{e,\rm exp}(\tilde{z}|\tilde{z}_e, s_\eta^2) = \frac{1}{2s_\eta(\tau)} exp\left[-\frac{|\tilde{z}-\tilde{z}_e|}{s_\eta(\tau)}\right] \tag{20a}$$

$$p_{e,\rm gau}(\tilde{z}|\tilde{z}_e, s_e^2) = \frac{1}{\sqrt{2\pi}s_e(\tau)} exp\left[-\frac{1}{2}\left(\frac{\tilde{z}-\tilde{z}_e}{s_e(\tau)}\right)^2\right] \tag{20b}$$

In Eqs. 20, s_η is the standard deviation of the mean bed height likely to increase with increasing bed shear stress (Eq. 18) as suggested by Wong et al. (2007); $\tilde{z}_e$ is an offset characterizing the position at which the maximum entrainment occurs, and s_e is the (bed shear stress dependent) standard deviation of the entrainment heights about the mean entrainment height.

For all simulations, we found p_e well-fit by Guassian distributions; not so well-fit by the exponential form (Eqs. 5b and 20a). Further, unlike that suggested by the exponential form, our fitted value of s_e appears to be independent of bed stress within the range we investigate (Table 3). In contrast, we found the distance of maximum entrainment $\tilde{z}_e$ from the mean bed height to increase with bed shear stress. We discuss the implications of our results in the following section.

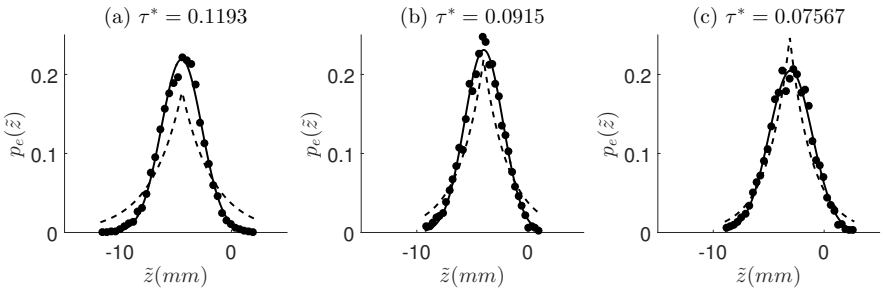

Figure 8. Three representative of entrainment height distributions. Filled circles represent the simulation data; the solid line represents a Gaussian fitting curve, $p_{e,gau}(\tilde{z}|\tilde{z}_e, s_e^2)$ (Eq. 20b), and the dashed line represents an exponential fitting curve, $p_{e,exp}(\tilde{z}|\tilde{z}_e, s_\eta^2)$, suggested by Wong et al. (2007), (Eq. 20a). Table 2 shows the fitting parameters from our data.

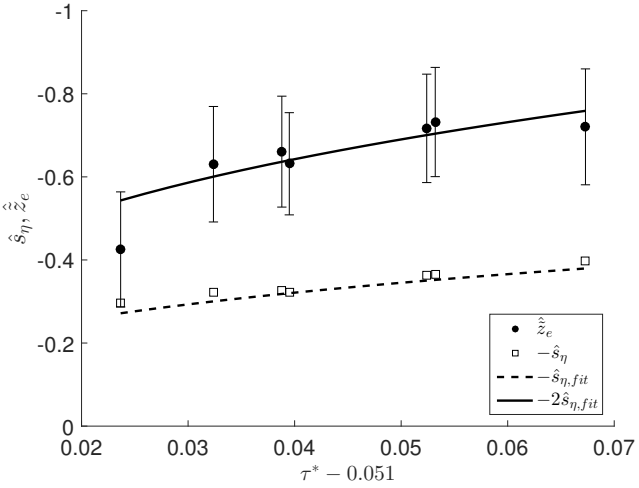

Figure 9. Normalized peak entrainment height, $\hat{\tilde{z}}_e$, and the normalized bed surface standard deviation, $\hat{s}_\eta$, as a function of excess Shields stress. Error bars show the normalized standard deviation of entrainment height distribution, $\hat{s}_e$ in Eq. 20b and table 3. $\hat{s}_{\eta,fit}$ is our power law fitting model for the bed surface standard deviations, Eq. 18 and Fig. 7.

Table 3. Summary of statistical analyses of bed surface for 7 computational experiments of this study. The statistical parameters are those found from fitted probability distributions to the data.

Run	τ^*	q^*	$\eta(mm)$	$\hat{s}_\eta$	$\hat{\tilde{z}}_e$	$\hat{s}_e$
1	0.1193	0.050	36.38	0.393	-0.71	0.255
2	0.1052	0.029	36.86	0.353	-0.77	0.276
3	0.1044	0.033	36.83	0.374	-0.73	0.254
4	0.0915	0.022	36.38	0.340	-0.70	0.238
5	0.0908	0.020	36.14	0.330	-0.69	0.270
6	0.0844	0.016	36.17	0.311	-0.62	0.254
7	0.0757	0.012	36.18	0.296	-0.46	0.281

5 Discussion

To understand the implications of the data presented above, we first compare them with experimental data obtained under similar boundary conditions. When considering the basic measure of average sediment flux (q^* vs. τ^* as in Eq. 15), our DEM model for bedload transport reproduces experimental transport measures remarkably well (Fig. 4(b)). In particular, the model Wong et al. (2007) derived for their experimental data represented our data almost perfectly (Table 4). Further, the reference stress we found below which the fit to our data indicates that minimal transport occurs (τ_c^*, Eq. 15) is close to that predicted by the analytical expression derived by Brownlie (1983) ($\tau_c^* = 0.053$) using previously published physical data (Shields, 1936). We propose that these similarities in the context of the relative simplicity of our simulations give strength to the strategy of using them for the statistical analysis we report in this paper and gaining a greater physics-based understanding of related behaviors (Hill & Tan, 2017).

Our bed surface variability showed that it was well-represented by a Gaussian distribution function, also similar to the form that emerged from the experiments by Wong

et al. (2007). As is true of the sediment flux, the standard deviation of the local bed height about the mean s_η increased with bed shear stress in the form of a power-law increase with excess Shields stress ($\tau^* - \tau_c^*$). This qualitative dependency was similar to that obtained experimentally by Wong et al. (2007). However, the results are quantitatively different as demonstrated by the plot in Fig. 7 and the fitted coefficients to Eq. 18 (Table 4). Namely, experimental standard deviation of the local bed height increases at a much higher rate than it does in the simulations.

We propose the differences in the bed-stress-dependence of the bed height variability is two-fold: (1) shape and associated significant of particle orientations and (2) measurement "techniques". Firstly, particle shape arguably plays a role in the type of interparticle contact that sustain particle assemblies. This is likely to be associated with increasing the differences of particle heights relative to neighboring particles. Along with this, bed height variability of a deposit of spherical particles is associated with the absolute height differences of the bed surface particle locations alone, while in a bed comprised of aspherical particles, bed surface variability may be due to both particle height and particle orientation of the topmost particles.

The second effect may be associated with what is essentially differences in measurement techniques. The bed height measurements by Wong et al. (2007) were obtained using ultrasound measurements of the local average of the topmost particle throughout their experiments, which likely includes at least some moving particles. In our simulations, the bed height measurements are based only on the top surface of the relatively stationary particles in the bed. New simulations with aspherical particles are underway to help us investigate the measurement differences and to test our hypotheses about the underlying differences between experimental and simulation results.

Table 4. Summary of fitted bed-stress dependence from Wong et al. (2007) experiments and our simulations (Eqs. 15 and 18).

results	a_q	τ_c^*	a_η	b_η
exp	2.66	0.55	3.09	0.56
sim	2.59	0.51	0.84	0.29

In contrast with the sediment flux and bed height variability, we could not compare entrainment height variability with the experimental results. Because of limited experimental measures, Wong et al. (2007) could only suggest, not measure, the experimental entrainment height variability. As a result our measures of entrainment height variability provide what we feel are the most significant insights of this work.

We highlight four significant entrainment height results: (i) First, the maximum probability of entrainment height did *not* coincide with the average bed surface in our simulations; (ii) the peak entrainment probability occurred *above* the average bed height in contrast of the proposal by Wong et al. (2007) that this maximum is likely *below* the average bed surface (Eq. 5b), and (iii) the entrainment height variability is well-represented by a Gaussian distribution function (Fig. 8) whose standard deviation of bed height variability ($\hat{s}_e = s_e/d_{50}$) does not vary monotonically or otherwise with τ_0 (Table 3).

(iv) Perhaps most significantly, the elevation at which the peak entrainment probability occurs ($\tilde{z}_e$) increases with increasing excess Shields stress, with a similar trend to the standard deviation of bed variability in Eq. 18. In fact, the highest rate of particle entrainment $|\tilde{z}_e| \sim 2s_\eta$ (Fig. 9). This makes intuitive sense as, effectively, the location from which particles are being "plucked" from the increases with the height of max-

imum protrusion of the bed into the flow. This result is promising in providing predictions of likely particle entrainment locations by knowing the hydraulic conditions.

To conclude this discussion, we reiterate the strength of this modeling technique not only for deriving probabilistic results for transport, but for a range of other questions such as recent data demonstrating anomalous transport and segregation (e.g., Viparelli et al. (2015)) and the size-dependence of increased mobility in beds of fine particles (e.g,. Hill et al. (2017)). We suspect that the trends we measured will vary significantly in a bimodal mixture of a different sizes and/or densities in a way that helps explain some of the segregation phenomenology whose origins remain elusive.

The very same simplifications that might be seen as limitations of the model, more importantly emphasize strengths of this approach. For example, for the results discussed here, there are no fluctuating fluid velocities. Rather, we represent the fluid forces on the bed using a steady local velocity whose profile is associated with previous measures of typical open channel turbulent flow. Thus, while there are limitations to the direct analogies we can make to specific turbulent effects here, we have shown some of the statistical variability that is driven by relatively simple particle interactions only. In the future, by turning on and off effects of velocity fluctuations, and different correlations in those velocity fluctuations, we can better determine the underlying physics of the phenomenology. The same thing can be said about particle sphericity, angularity, and other details of shape sometimes that arguably contribute significantly to the phenomenology. By using relatively simplistic simulations such as those described here, one can systematically vary these and other particle parameters to obtain a physics-based quantitative understanding of observed variations in streambeds and other sedimentary structures. One can use this framework to investigate transport-changing details in bedload transport including time-dependent bed aging measured in sub-bedload conditions and repeated flood events (e.g., Phillips et al. (2018) and Masteller et al. (2019)). And, finally, we expect this will allow us to link to literature often referred to as *granular physics* including long-range force chains (or correlations in interparticle contact forces) and other details of fabric.

6 Summary and Future Work

To summarize, we used Distinct Element Method (DEM) simulations to investigate relationships between average shear stress at the bed, bed surface height statistics, and bed entrainment statistics for particles in bedload transport under lower plain bed conditions. Toward isolating effects of shear stress magnitude from other natural variabilities, we represented the phenomenology within a relatively simple physics-based simulation framework. For validation purposes, our particle size distribution followed published experimental work, specifically, the log-normal gravel particle size distribution of experiments performed by Wong et al. (2007). Simplifications included particle shape (spheres) and flow conditions (a unidirectional logarithmic average flow profile), where the representation of the bed shear stress appeared in the variation of fluid velocity $\overline{u}_f(z)$ with distance from the bed z: $d\overline{u}_f(z)/dz = u_\tau/(\kappa z) = \sqrt{\tau_o/\rho_\mathrm{f}}/(\kappa z)$.

We found these simulations reproduced much of the transport data from previously published experimental results. Specifically: (1) The value of $\tau_c^* \sim 0.051$, is comparable with that of other bedload transport models such as those by Ashida and Michiue (1972), Luque and Van Beek (1976), Engelund and Fredsøe (1976), and Wong and Parker (2006), and (2) The dependence of bed transport on average shear stress increases as a power law of excess shear stress according to $q^* \sim (\tau^* - \tau_c^*)^{3/2}$, similar to well-established transport laws (Meyer-Peter & Muller, 1948; Ashida & Michiue, 1972) and nearly identical to that obtained from experiments after which we modeled our simulations (Wong et al., 2007).

Our most significant new results involve a robust relationship between local bed height statistics and maximum entrainment probability. Using a well-defined definition of local computational bed-surface height, we found that bed height statistics are well-represented by a Gaussian distribution as obtained experimentally by Wong et al. (2007) and whose standard deviation increases with excess Shields stress: $s_\eta = 0.84 d_{50} (\tau^* - 0.051)^{0.29}$. In contrast, the standard deviation of entrainment height distribution shows no correlation with the Shields stress. Rather, the height from which the most particles are entrained increases with bed shear stress as well, $\tilde{z}_e \approx 2 s_\eta$ above the average bed height for all runs.

These results have established how powerful that simplified DEM simulations can be in representing transport details while, at the same time, they have the ability to isolate dynamics in a manner often inaccessible to experiments. Using such a simple model as the simulation we describe here, we can turn on and off a variety of *phenomenology* ranging from turbulent fluctuations in the fluid to asphericity and irregularity in particles shapes and sizes. Toward this, next steps in our work involve additional simulations we are using to better understand effects of such dynamics including fluctuating velocities as appears with true turbulent conditions, particle size variations, and particle asphericity.

References

Abbott, J., & Francis, J. R. D. (1977). Saltation and suspension trajectories of solid grains in a water stream. *Philosophical Transactions of the Royal Society of London. Series A, Mathematical and Physical Sciences*, *284*(1321), 225–254.

Ashida, K., & Michiue, M. (1972). Study on hydraulic resistance and bed-load transport rate in alluvial streams [in Japanese]. In *Proceedings of the Japan Society of Civil Engineers* (pp. 59–69).

Bagnold, R. A. (1956). The flow of cohesionless grains in fluids. *Philosophical Transactions of the Royal Society of London. Series A, Mathematical and Physical Sciences*, *249*(964), 235–297.

Batchelor, G. K. (1976). *An introduction to fluid dynamics*. Cambridge, UK: Cambridge university press.

Blom, A., Ribberink, J. S., & Parker, G. (2008). Vertical sorting and the morphodynamics of bed form-dominated rivers: A sorting evolution model. *Journal of Geophysical Research: Earth Surface*, *113*(F1). doi: 10.1029/2003JF000069

Bridge, J., & Dominic, D. (1984). Bed load grain velocities and sediment transport rates. *Water Resources Research*, *20*(4), 476–490. doi: 10.1029/WR020i004p00476

Brownlie, W. R. (1983). Flow depth in sand-bed channels. *Journal of Hydraulic Engineering*, *109*(7), 959–990.

Chapra, S. C., Canale, R. P., et al. (2010). *Numerical methods for engineers*. Boston: McGraw-Hill Higher Education,.

Cui, Y., Braudrick, C., Dietrich, W. E., Cluer, B., & Parker, G. (2006). Dam removal express assessment models (dream) part 2: Sample runs/sensitivity tests. *Journal of Hydraulic Research*, *44*(3), 308–323. doi: 10.1080/00221686.2006.9521684

Cui, Y., Parker, G., Braudrick, C., Dietrich, W. E., & Cluer, B. (2006). Dam removal express assessment models (dream). part 1: model development and validation. *Journal of Hydraulic Research*, *44*(3), 291–307. doi: 10.1080/00221686.2006.9521683

Cundall, P. A., & Strack, O. D. (1979). A discrete numerical model for granular assemblies. *geotechnique*, *29*(1), 47–65.

Drake, T. G., & Calantoni, J. (2001). Discrete particle model for sheet flow sediment transport in the nearshore. *Journal of Geophysical Research: Oceans*, *106*(C9),

19859–19868. doi: 10.1029/2000JC000611

Engelund, F., & Fredsøe, J. (1976). A sediment transport model for straight alluvial channels. *Hydrology Research*, *7*(5), 293–306.

Ferguson, R. I. (2003). Emergence of abrupt gravel to sand transitions along rivers through sorting processes. *Geology*, *31*(2), 159–162. doi: 10.1130/0091-7613(2003)031⟨0159:EOAGTS⟩2.0.CO;2

Hertz, H. (1882). Ueber die berührung fester elastischer körper. journal für die reine und angewandte mathematik. *Crelles Journal*, *92*, 156–171.

Hill, K. M., Gaffney, J., Baumgardner, S., Wilcock, P., & Paola, C. (2017). Experimental study of the effect of grain sizes in a bimodal mixture on bed slope, bed texture, and the transition to washload. *Water Resources Research*, *53*(1), 923–941.

Hill, K. M., & Tan, D. (2017). Granular flows applied to gravel-bed rivers: particle-scale studies of the mobilization of a gravel bed by the addition of fines. In D. Tsutsumi & J. B. Laronne (Eds.), *Gravel-bed rivers: Processes and disasters* (pp. 73–95). Wiley Online Library. doi: 10.1002/9781118971437.ch3

Hirano, M. (1971). River-bed degradation with armoring. In *Proceedings of the japan society of civil engineers* (Vol. 1971, pp. 55–65).

Luque, R. F., & Van Beek, R. (1976). Erosion and transport of bed-load sediment. *Journal of hydraulic research*, *14*(2), 127–144.

Masteller, C. C., Finnegan, N. J., Turowski, J. M., Yager, E. M., & Rickenmann, D. (2019). History-dependent threshold for motion revealed by continuous bedload transport measurements in a steep mountain stream. *Geophysical Research Letters*, *46*(5), 2583–2591.

Meyer-Peter, E., & Muller, R. (1948). Formulas for bed-load transport. In *Proceedings of the 2nd meeting of the International Association for Hydraulic Structures Research* (pp. 39–64). Stockholm, Sweden: International Association for Hydraulic Structures Research.

Mindlin, R. D. (1949). Compliance of elastic bodies in contact. *ASME Journal of Applied Mechanics*, *16*, 259–268.

Parker, G. (1991a). Selective sorting and abrasion of river gravel. ii: Applications. *Journal of Hydraulic Engineering*, *117*(2), 150–171. doi: 10.1061/(ASCE)0733-9429(1991)117:2(150)

Parker, G. (1991b). Selective sorting and abrasion of river gravel. i: Theory. *Journal of Hydraulic Engineering*, *117*(2), 131–147. doi: 10.1061/(ASCE)0733-9429(1991)117:2(131)

Parker, G. (2004). 1d sediment transport morphodynamics with applications to rivers and turbidity currents. *E-book available from http://vtchl. uiuc. edu/people/parkerg/morphodynamics_e-book. htm (last accessed 23 February 2010)*.

Parker, G., Paola, C., & Leclair, S. (2000). Probabilistic exner sediment continuity equation for mixtures with no active layer. *Journal of Hydraulic Engineering*, *126*(11), 818–826. doi: 10.1061/(ASCE)0733-9429(2000)126:11(818)

Pelosi, A., Parker, G., Schumer, R., & Ma, H.-B. (2014). Exner-based master equation for transport and dispersion of river pebble tracers: Derivation, asymptotic forms, and quantification of nonlocal vertical dispersion. *Journal of Geophysical Research: Earth Surface*, *119*(9), 1818–1832. doi: 10.1002/2014JF003130

Phillips, C., Hill, K. M., Paola, C., Singer, M., & Jerolmack, D. (2018). Effect of flood hydrograph duration, magnitude, and shape on bed load transport dynamics. *Geophysical Research Letters*, *45*(16), 8264–8271.

Pope, S. B. (2001). *Turbulent flows*. IOP Publishing.

Ribberink, J. S. (1987). Mathematical modelling of one-dimensional morphological changes in rivers with non-uniform sediment.

Savage, S., & Lun, C. (1988). Particle size segregation in inclined chute flow of dry cohesionless granular solids. *Journal of Fluid Mechanics*, *189*, 311–335.

Schlichting, H., & Gersten, K. (2016). *Boundary-layer theory*. Springer.

Schmeeckle, M. W., & Nelson, J. M. (2003). Direct numerical simulation of bedload transport using a local, dynamic boundary condition. *Sedimentology*, *50*(2), 279–301. doi: 10.1046/j.1365-3091.2003.00555.x

Shields, A. (1936). Anwendung der aehnlichkeitsmechanik und der turbulenzforschung auf die geschiebebewegung. *PhD Thesis Technical University Berlin*.

Tsuji, Y., Tanaka, T., & Ishida, T. (1992). Lagrangian numerical simulation of plug flow of cohesionless particles in a horizontal pipe. *Powder technology*, *71*(3), 239–250. doi: 10.1016/0032-5910(92)88030-L

van Rijn, L. C. (1982). Equivalent roughness of alluvial bed. *Journal of the Hydraulics Division*, *108*(10), 1215–1218.

Viparelli, E., Haydel, R., Salvaro, M., Wilcock, P. R., & Parker, G. (2010). River morphodynamics with creation/consumption of grain size stratigraphy 1: laboratory experiments. *Journal of Hydraulic Research*, *48*(6), 715–726. doi: 10.1080/00221686.2010.515383

Viparelli, E., Sequeiros, O. E., Cantelli, A., Wilcock, P. R., & Parker, G. (2010). River morphodynamics with creation/consumption of grain size stratigraphy 2: numerical model. *Journal of Hydraulic Research*, *48*(6), 727–741. doi: 10.1080/00221686.2010.526759

Viparelli, E., Solari, L., & Hill, K. (2015). Downstream lightening and upward heavying: Experiments with sediments differing in density. *Sedimentology*, *62*(5), 1384–1407.

Wilcock, P. R., & Crowe, J. C. (2003). Surface-based transport model for mixed-size sediment. *Journal of Hydraulic Engineering*, *129*(2), 120–128. doi: 10.1061/(ASCE)0733-9429(2003)129:2(120)

Wong, M., & Parker, G. (2006). Reanalysis and correction of bed-load relation of meyer-peter and müller using their own database. *Journal of Hydraulic Engineering*, *132*(11), 1159–1168.

Wong, M., Parker, G., DeVries, P., Brown, T. M., & Burges, S. J. (2007). Experiments on dispersion of tracer stones under lower-regime plane-bed equilibrium bed load transport. *Water Resources Research*, *43*. doi: 10.1029/2006WR005172

Appendix A

This section shows how we calculate the contact parameters used in Eq. 7. These parameters are determined from the characteristics (e.g., radius, elastic and shear modules) of the particles in contact by the following equations:

$$k_n = \frac{4}{3}\sqrt{r_{\text{eff}}}E_{\text{eff}} \tag{A1a}$$

$$k_t = 8\sqrt{r_{\text{eff}}}G_{\text{eff}} \tag{A1b}$$

$$\eta_n = \alpha\sqrt{m_{\text{eff}}k_n} \tag{A1c}$$

$$\eta_t = \alpha\sqrt{m_{\text{eff}}k_t} \tag{A1d}$$

where R_{eff}, m_{eff}, E_{eff}, G_{eff} are the effective radius, mass, elastic modulus and shear modulus, respectively. α is equal to 0.07 for the coefficient of restitution ~ 0.9 used in this study according to Tsuji et al. (1992). We determine the effective radius, mass, elas-

tic modulus and shear modulus by the following equations where r_1, ν_1, E_1, m_1, r_2, ν_2, E_2 and m_2 are the radius, Poisson's ratio, elastic modulii and mass of the particles 1 and 2 that are in contact with each other.

$$r_{\text{eff}} = \left(\frac{1}{r_1} + \frac{1}{r_2}\right)^{-1} \tag{A2a}$$

$$E_{\text{eff}} = \left(\frac{1-{\nu_1}^2}{E_1} + \frac{1-{\nu_2}^2}{E_2}\right)^{-1} \tag{A2b}$$

$$G_{\text{eff}} = \left(\frac{2(1+\nu_1)(2-\nu_1)}{E_1} + \frac{2(1+\nu_2)(2-\nu_2)}{E_2}\right)^{-1} \tag{A2c}$$

$$m_{\text{eff}} = \left(\frac{1}{m_1} + \frac{1}{m_2}\right)^{-1} \tag{A2d}$$

Notation

$\boldsymbol{A}$ Central cross-sectional area of a particle $[m^2]$
$\boldsymbol{a_q}$ Fitting parameter to relate transport rate to Shields stress (see Eq. 15) [-]
$\boldsymbol{a_u}$ Coefficient that determine a velocity threshold (see Eq. 16) [-]
$\boldsymbol{a_\eta}$ Fitting parameter to relate standard deviation of bed surface variations to Shields stress (see Eq. 18) [-]
$\boldsymbol{b_\eta}$ Fitting parameter to relate standard deviation of bed surface variations to Shields stress (see Eq. 18) [-]
$\boldsymbol{c_d}$ Drag coefficient [-]
$\boldsymbol{c_m}$ Added mass coefficient [-]
$\boldsymbol{D}$ Volumetric sediment deposition rate per unit area at a particular location (x,z) $[m/s]$
$\boldsymbol{D_i}$ Volumetric sediment deposition rate of particles of type i per unit area $[m/s]$
$\boldsymbol{d_{50}}$ Median particle size [m]
$\boldsymbol{d_g}$ Geometric mean particle size [m]
$\boldsymbol{d}$ Particle Diameter [m]
$\boldsymbol{E}$ Volumetric sediment entrainment rate per unit area at a particular location (x,z) $[m/s]$
$\boldsymbol{E_p}$ Particle modulus of elasticity $[N/m^2]$
erf Error function. For variable "x" the error function is defined as: $erf(x) = \frac{1}{\sqrt{\pi}} \int_{-x}^{x} e^{-t^2} dt$
$\vec{\boldsymbol{F}}_{\boldsymbol{b}}$ Buoyancy force [N]
$\vec{\boldsymbol{F}}^{\boldsymbol{c}}$ Interparticle contact force [N]
$\vec{\boldsymbol{F}}_{\boldsymbol{d}}$ Drag Force [N]
$\vec{\boldsymbol{F}}^{\boldsymbol{f}}$ Fluid force [N]
$\vec{\boldsymbol{F}}^{\boldsymbol{g}}$ Gravity force [N]
$\vec{\boldsymbol{F}}_{\boldsymbol{m}}$ Added mass force [N]
$\vec{\boldsymbol{F}}_{\boldsymbol{n}}$ Component of interparticle contact force normal to an interparticle contact plane in the DEM model [N]
$\vec{\boldsymbol{F}}^{\boldsymbol{nc}}$ Interparticle non-contact force [N]
$\vec{\boldsymbol{F}}_{\boldsymbol{p}}$ Sum of all forces on a particle defined by Eq. 8 [N]
$\vec{\boldsymbol{F}}_{\boldsymbol{t}}$ Component of interparticle force tangential to an interparticle contact plane in the DEM model [N]
$\boldsymbol{f_{a,i}}$ Volume fraction of particles of type i in the active layer.
$\boldsymbol{f_{L,i}}$ Volume fraction of particles of type i at the interface between active layer and substrate.
$\boldsymbol{g}$ Gravitational acceleration ($= 9.81$) $[m/s^2]$
$\boldsymbol{h}$ Local bed height (see Fig. 1) [m]
$\boldsymbol{h_p}$ Height difference between the topmost part of two particles (see Eq. 11) [m]

669 $\boldsymbol{I_i}$ Moment of inertia of particle i
670 $\boldsymbol{i}$ Particle counter
671 $\boldsymbol{k_n}$ Normal stiffness factor (see Eq. 7) $[N/m^{1.5}]$
672 $\boldsymbol{k_s}$ Roughness length-scale ($= 3.5d_{50}$) [m]
673 $\boldsymbol{k_t}$ Tangential stiffness factor (see Eq. 7) $[N/m]$
674 $\boldsymbol{L}$ Representative length scale [m]
675 $\boldsymbol{L_a}$ Active layer thickness [m]
676 $\boldsymbol{\hat{L}}$ Dimensionless length scale [-]
677 $\boldsymbol{l_d}$ Downstream distance between the center of two particles (see Eq. 11) [m]
678 $\boldsymbol{M}$ Torque $[kgm^2/t^2]$
679 $\boldsymbol{m_i}$ Mass of particle i
680 $\boldsymbol{N}$ Number of particles
681 $\boldsymbol{p_d}$ Probability density of deposition rate (see Eq. 3 and 5a) [-]
682 $\boldsymbol{p_e}$ Probability density of entrainment rate (see Eq. 3 and 5b) [-]
683 $\boldsymbol{p_\eta}$ Probability density of bed height (see Eq. 4) [-]
684 $\boldsymbol{q}$ Volumetric sediment transport rate per unit width $[m^2/s]$
685 $\boldsymbol{q_{t_i}}$ Volumetric sediment transport rate of the simulation data at output time step t_i (see
686 Eq. 12) $[m^2/s]$
687 $\boldsymbol{q^*}$ Dimensionless sediment transport rate (see Eq. 13) [-]
688 $\boldsymbol{q^*_{20}}$ Average dimensionless sediment transport rate for 20 seconds after steady-state trans-
689 port rate [-]
690 $\boldsymbol{q^*_T}$ Average dimensionless sediment transport rate from t_s to $T = t - t_s$ [-]
691 $\boldsymbol{q^*_{\mathrm{fit}}}$ Dimensionless sediment transport rate proposed by authors for this study $q^*_{\mathrm{fit}} =$
692 $2.59(\tau^* - 0.051)^{1.5}$ [-]
693 $\boldsymbol{q^*_{\mathrm{flv}}}$ Dimensionless sediment transport rate proposed by Luque and Van Beek (1976) $q^*_{\mathrm{flv}} =$
694 $5.7(\tau^* - 0.06)^{1.5}$ [-]
695 $\boldsymbol{q^*_{\mathrm{mpm}}}$ Dimensionless sediment transport rate proposed by Meyer-Peter and Muller (1948)
696 and modified by Wong and Parker (2006) $q^*_{\mathrm{mpm}} = 3.97(\tau^* - 0.0495)^{1.5}$ [-]
697 $\boldsymbol{q^*_{\mathrm{sim}}}$ Dimensionless sediment transport rate from the simulations of this study (see Fig.
698 4) [-]
699 $\boldsymbol{q^*_{t_i}}$ Dimensionless sediment transport rate at output time step t_i [-]
700 $\boldsymbol{q^*_{\mathrm{wpdbb}}}$ Dimensionless sediment transport rate proposed by Wong $q^*_{\mathrm{wpdbb}} = 2.66(\tau^* -$
701 $0.0549)^{1.5}$ [-]
702 $\boldsymbol{Re_p}$ Particle Reynolds number [-]
703 $\boldsymbol{s}$ Particle specific gravity [-]
704 $\boldsymbol{s_e}$ Standard deviation of the entrainment height [m]
705 $\boldsymbol{s_\eta}$ Standard deviation of bed surface variations [m]
706 $\boldsymbol{\hat{s}_\eta}$ Normalized standard deviation of bed surface variations by median particle size [-
707]
708 $\boldsymbol{T}$ Physical time starting just after steady-state transport [s]
709 $\boldsymbol{t}$ Physical time [s]
710 $\boldsymbol{t_s}$ Physical time to reach the steady-state transport. For the simulations of this study
711 t_s is 2.5 seconds [s]
712 $\boldsymbol{t_i}$ Output time step of DEM model [s]
713 $\boldsymbol{u_{\mathrm{bd}}}$ Velocity of bed particles [m/s]
714 $\boldsymbol{\vec{u}_{f,x}}$ Fluid velocity in the downstream direction [m/s]
715 $\boldsymbol{\vec{u}}$ Particle velocity [m/s]
716 $\boldsymbol{\vec{u}_x}$ Particle velocity component in downstream direction [m/s]
717 $\boldsymbol{\vec{u}_y}$ Particle velocity component in cross-stream direction [m/s]
718 $\boldsymbol{\vec{u}_z}$ Particle velocity component in vertical direction [m/s]
719 $\boldsymbol{\vec{u}_{\mathrm{rel}}}$ Relative velocity between particle and fluid $(\vec{u}_f - \vec{u})$[m/s]
720 $\boldsymbol{\vec{u}_{\mathrm{rel},x}}$ Relative velocity between particle and fluid in downstream direction $(\vec{u}_{f,x} - \vec{u}_x)$[m/s]

721 $\vec{u}_{rel,y}$ Relative velocity between particle and fluid in cross-stream direction ($\vec{u}_{f,y}-\vec{u}_y$)[m/s]
722 $\vec{u}_{rel,z}$ Relative velocity between particle and fluid in cross-stream direction ($\vec{u}_{f,z}-\vec{u}_z$)[m/s]
723 u_{th} Threshold velocity to distinguish between moving and stationary particles (see Eq.
724 17) [m/s]
725 u_τ Shear velocity ($u_\tau = \sqrt{\tau_0/\rho}$) [m/s]
726 $u_{\tau c}$ Critical shear velocity [m/s]
727 x Coordinate in the downstream direction [m]
728 y Coordinate in the cross-stream direction [m]
729 z Coordinate in the upward direction [m]
730 z_0 Position in the bed at which the fluid velocity is zero in the log-law in the DEM model
731 (see Fig. 2) [m]
732 z_1 Distance between the bed surface and zero-fluid-velocity plane ($z_1 = 2d_{50}$) [m]
733 z_c Vertical location of a particle center [m]
734 $z_{top,i,j}$ Topmost part of particle i on the bed surface in column j [m]
735 $\tilde{z}$ Coordinate in the downward direction with reference located at the mean bed height:
736 ($\tilde{z} = \eta - z$) [m]
737 $\tilde{z}_e$ Offset distance associated with mobile-bed equilibrium and representing the height
738 of the maximum entrainment rate (see Eq. 5 and Eq. 20) [m]
739 $\tilde{z}_n$ Offset distance associated with non-equilibrium conditions (see Eq. 5) [m]
740 δ_n Representative deformation normal to the contact plane of an interparticle contact
741 in the DEM model [m]
742 $\dot{\delta}_n$ Temporal derivative of δ_n [m/s]
743 δr_{min} Minimum displacement of a particle from stationary status to be considered as
744 an eroded particle (see Eq. 19) [m]
745 δ_t Representative deformation tangential to the contact plane of an interparticle con-
746 tact in the DEM model [m]
747 $\dot{\delta}_t$ Temporal derivative of δ_t [m/s]
748 η Mean bed height (see Fig. 1) [m]
749 η_n Damping coefficient associated with compressive deformation of a particle (see Eq.
750 7) [$Nt/m^{5/4}$]
751 η_t Damping coefficient associated with shear deformation of a particle (see Eq. 7) [$Nt/m^{5/4}$]
752 κ Von Karman constant [-]
753 λ_p Bed porosity [-]
754 μ Interparticle friction coefficient [-]
755 ν Kinematic viscosity of fluid [m^2/s]
756 ν_p Particle Poisson ratio [-]
757 ρ_f Fluid mass density [kg/m^3]
758 ρ_p Particle mass density [kg/m^3]
759 σ_g Geometric standard deviation of particle size distribution [-]
760 τ Shear stress [N/m^2]
761 τ_0 Bed shear stress [N/m^2]
762 τ^* Shields stress [-]
763 τ_c^* Critical Shields stress [-]
764 $\forall_i$ Volume of particle i [m^3]
765 ω_i Rotational velocity of particle i [$1/s$]

766 **Acknowledgments**
767 We thank the Army Research Office (ARO) for funding this research under the grant
768 W911NF-16-1-0337. This link (we will provide it upon acceptance) provides access to
769 the data used in this study.